

Article

Displacement Analyses of Diaphragm Wall in Small-Scale Deep Excavation Considering Joints between Panels

Ming Yang ¹, Rongxing Wu ¹ , Chenxi Tong ^{2,*}, Jianwei Chen ³ and Bing Tang ⁴

¹ Institute of Applied Mechanics, Ningbo Polytechnic, Ningbo 315800, China; yangming@nbpt.edu.cn (M.Y.); wurongxing98@163.com (R.W.)

² School of Civil Engineering, Central South University, Changsha 410075, China

³ Research Center of Integrated Pipe Gallery, Ningbo Urban Construction Design & Research Institute Co., Ltd., Ningbo 315012, China; jave0401@163.com

⁴ Institute of Architecture and Urban Planning, China Railway Siyuan Survey and Design Group Co., Ltd., Wuhan 430063, China; 006251@crfsdi.com

* Correspondence: cxtong@csu.edu.cn

Abstract: This paper proposed a new method for modelling joints, using anisotropic plate elements and elastic bar elements to address the issue that joints between panels are usually disregarded in numerical modelling. For small-scale deep excavations, which are frequently performed in the construction of various working shafts but have not been sufficiently studied, two numerical models were developed, using the No.1 Shaft of Tongtu Road Utility Tunnel in Ningbo, China, as a research object. One model considered the joints between the panels as proposed, while the other disregarded the joints as conventional. In comparison to the conventional method, the proposed method was validated due to yielding wall displacements that closely matched the results of the field monitoring, with a notable reduction in the error observed in the calculated displacements for the short side of the excavation. Furthermore, 34 numerical models were developed in order to investigate the influence of excavation length, depth, and diaphragm wall thickness on the relative differences between the calculated displacements obtained by the two models. The results of this study can provide references for the development of finite element models for designing small-scale deep excavation.

Keywords: small-scale deep excavation; diaphragm walls; joints; numerical modelling; field monitoring



Citation: Yang, M.; Wu, R.; Tong, C.; Chen, J.; Tang, B. Displacement Analyses of Diaphragm Wall in Small-Scale Deep Excavation Considering Joints between Panels. *Buildings* **2024**, *14*, 1449. <https://doi.org/10.3390/buildings14051449>

Received: 18 April 2024

Revised: 6 May 2024

Accepted: 13 May 2024

Published: 16 May 2024



Copyright: © 2024 by the authors. Licensee MDPI, Basel, Switzerland. This article is an open access article distributed under the terms and conditions of the Creative Commons Attribution (CC BY) license (<https://creativecommons.org/licenses/by/4.0/>).

1. Introduction

Deep excavation is an essential phase in the development of underground space in urban areas and diaphragm walls, which are configured by separate wall panels and vertical joints between panels, are widely used to brace excavations owing to the high rigidity, good integrity, and impermeability of the walls themselves [1–5]. In comparison to the deep excavations commonly encountered in the construction of high-rise buildings and subway stations, which have considerable plan size, the small-scale deep excavations investigated in this paper have length and widths that are not much larger, and sometimes even smaller, than the excavation depth. It is expected that this excavation will have a significant spatial effect because of its small aspect ratio [6]. As is shown in Table 1, small-scale deep excavations braced by diaphragm walls are commonly used to construct working shafts that serve as launching platforms for tunnel-boring machines in various traffic and municipal engineering projects, particularly in China.

Numerous studies have been carried out to investigate the performance of deep excavations braced by diaphragm walls with struts in recent decades [7–11]. To ensure the safety of deep excavations and the surrounding environment, it is crucial for practical engineers to pay close attention to the horizontal displacement of the diaphragm walls, particularly the maximum displacement [12,13], as well as the precise location of underground utilities in the vicinity of the excavations [14,15]. Numerical modelling has been commonly used

to predict the displacement of the diaphragm walls during the excavation process [16–20]. Guo et al. [21] used the finite difference method to analyse the deflections of a deep metro station excavation braced by diaphragm walls under unsymmetrical surcharge effects. Schwamb et al. [22] conducted numerical analyses to investigate the performance of a circular shaft during construction. Pedro et al. [23] evaluated the impact of an elliptical deep excavation on the surrounding buildings using 3D finite element analysis. However, the majority of the previous studies did not concentrate on the small-scale deep excavations mentioned above. Furthermore, the joints between panels were typically disregarded in numerical modelling, despite the fact that these joints have a significant impact on the wall performance [24,25].

Table 1. Cases of small-scale deep excavations braced by diaphragm walls.

Case	Length (m)	Width (m)	Depth (m)	Time
Shaft of Jintang Subsea Tunnel of Ningbo–Zhoushan Railway in Ningbo	22.6	21.1	58.13	2024
No. 3 shaft of Metro Line 16 co-constructed with pipe gallery in Shenzhen	32	15	27.58	2023
Launching shaft of metro rail project in Dhaka	20	20	17	2023
No. 1 shaft of Yinzhou Road utility tunnel in Ningbo	32.6	14.6	18.12	2021
Launching shaft of Pearl River estuary tunnel of Shenzhen–Jiangmen railway in Guangzhou	23.4	26.8	25.35	2021
Fujian North Road shaft of Beiheng channel in Shanghai	23	22	29.35	2021
Jingfangyuan stereo garage in Hangzhou	22.4	10.8	46.2	2020
No. 2 and No. 3 shaft of Wanjiali Road power tunnel in Changsha	33.8	10.6	20.2	2018
South shaft and North shaft of Sutong GIL utility tunnel in Suzhou and Nantong, respectively	18.8	10	24.8	
South shaft and North shaft of Sutong GIL utility tunnel in Suzhou and Nantong, respectively	32	22.85	20.85	2017
Rákóczi square station of the 4th metro line in Budapest	30	23.5	29.25	
Launching platform of Moorgate station in Crossrail route in London	53.4	27.9	27.9	2014
Launching platform of Moorgate station in Crossrail route in London	33	33	40.7	2005

Referring to the modelling of joints between panels in numerical analysis, limited numbers of researchers conducted relevant studies. Zdravkovic et al. [26] and Dong et al. [25,27,28] treated the diaphragm walls as an integrated panel, which was simulated using anisotropic solid elements or anisotropic shell elements, and then reduced its horizontal stiffness due to the joints between panels. However, this was inconsistent with the fact that the diaphragm walls were composed of several discrete wall panels, which were homogeneous and isotropic, and the reduced ratio had to be determined on a trial-and-error basis, which is not supported by theory. Chen et al. [29] simulated the steel plates of the cross-plate joint and the reinforced concrete using solid elements, and the interaction between the steel plate and the reinforced concrete was modelled using interface elements. However, the modelling process is relatively time-consuming, and structural forces of diaphragm walls have to be calculated from the stresses at element integration points, which makes the whole process cumbersome in a practical design situation. For the aforementioned reasons, the joints between panels were typically disregarded in numerical modelling [16–23].

To address the two issues mentioned above, this study first proposed a convenient and practical method for modelling joints, and then analysed the displacement behavior of diaphragm walls in small-scale deep excavation by considering the joints between panels. The investigated deep excavation of the No.1 Shaft of Tongtu Road Utility Tunnel was built with the purpose of launching new tunnel excavation fronts for a utility tunnel in Ningbo, China. In this paper, the joints between panels were simulated with anisotropic plate elements and elastic bar elements, which are commonly employed in numerical modelling, and numerical models considering and disregarding the joints were developed respectively. Better agreement was found between the field data and the results when the joints were considered as proposed, in contrast to the results obtained when the joints were disregarded as conventional, and a notable reduction in the error was observed in the calculated displacements for the short side of the excavation when the joints were

considered as proposed, which indicated the effectiveness of the proposed method and the necessity of considering the joints. Finally, numerical models were developed to investigate the influence of excavation length, depth, and diaphragm wall thickness on the relative differences between the calculated displacements obtained by the two models. The results of this study can provide references for the development of finite element models for the design of small-scale deep excavation.

2. Basic Information Regarding the Investigated Deep Excavation

The investigated deep excavation for Tongtu Road Utility Tunnel is located in the Yinzhou Area of Ningbo, China, and it serves as a starting shaft for launching a tunnel-boring machine. As shown in Figures 1 and 2, the deep excavation area has a depth of 16.8 m, with a length of 46.6 m and a width of 14.5 m. The designed supporting schemes consist of diaphragm walls with five strut levels, placed at elevations of 1.91, -1.79 , -4.79 , -7.79 , and -10.79 m, respectively. The diaphragm wall has a thickness of 0.8 m and a depth of 30.42 m. The reinforced concrete structure is employed for the first struts, with cross-sections of $700 \times 700 \text{ mm}^2$. The other struts are steel pipes, and the cross-section of the steel pipes has an external diameter of 609 mm and 800 mm, respectively, for the second struts and the remaining struts, and the thickness of all steel pipes is 16 mm. The Young's moduli, E , of the concrete and steel used at this site are 31.5 GPa and 200 GPa, respectively.

The soil profile obtained from the geological survey is depicted in Figure 2. There were nine soil layers from the ground surface to the toe of the diaphragm wall. The first layer from the ground surface was miscellaneous fill (MF), with a thickness of 1.68 m. The second to ninth layers were clay, mucky clay, silty clay, silty sand, silty clay with silty sand (SCSS), mucky silty clay (MSC), clay, and silty clay. The remaining soil layers and their thicknesses, from the toe of the diaphragm wall to the bottom of the model, are listed in Table 2, and the water table is located between 1.5 m and 1.7 m below the ground surface.

Table 2. Basic HSS model parameters used in the excavation.

Soil Layer	Thickness (m)	γ ($\text{kN} \cdot \text{m}^{-3}$)	e	E_{s1-2} (MPa)	c' (kPa)	ϕ' ($^\circ$)
① _{1a} MF	1.50	20.0	0.950	3.40	1.0	8.0
① ₂ Clay	1.28	18.3	1.067	3.80	3.5	24.6
① _{3b} Mucky clay	1.92	17.3	1.368	2.46	8.8	26.6
② _{2b} Silty clay	11.28	17.0	1.458	2.24	7.0	25.6
③ _{1b} Silty sand	3.04	19.6	0.724	10.95	4.0	25.4
③ ₂ SCSS	3.46	18.8	0.838	6.02	9.1	29.0
④ _{1b} MSC	1.69	18.3	1.030	3.52	6.2	29.8
⑤ _{1a} Clay	2.91	19.3	0.824	8.06	8.0	28.7
⑤ ₂ Silty clay	5.40	19.0	0.878	6.05	20.0	25.6
⑤ _{3a} Clayey silt	1.90	19.0	0.808	8.92	4.6	29.5
⑤ _{3t} Silty clay	5.90	18.7	0.969	5.49	5.3	31.0
⑥ _{2t} Clayey silt	3.10	19.0	0.849	8.19	7.8	33.6
⑥ ₂ Silty clay	2.20	18.5	0.992	4.51	15.7	27.7
⑥ _{3a} Clay	4.40	19.5	0.822	10.64	2.7	31.0
⑦ ₂ silty clay	5.81	18.9	0.887	4.92	3.9	32.9
Soil cement	-	20.0	-	-	60.0	25.0

Note: MF = miscellaneous fill; MSC = mucky silty clay; SCSS = silty clay with silty sand; interface strength reduction $R_{\text{inter}} = 0.67$.

As shown in Figures 1 and 2, soil cement columns of 14.5 m in length, 3.0 m or 3.8 m in width, and 3.0 m in thickness were used to improve the ground at the bottom of the excavation. The east ground of the excavation was reinforced by soil cement columns, measuring 12.7 m in length, 8.5 m in width, and 12.7 m in thickness, to ensure the safety of launching the tunnel-boring machine. In the following sections, the east and west sides are referred to as the short side, while the north and south sides are referred to as the long side for convenience.

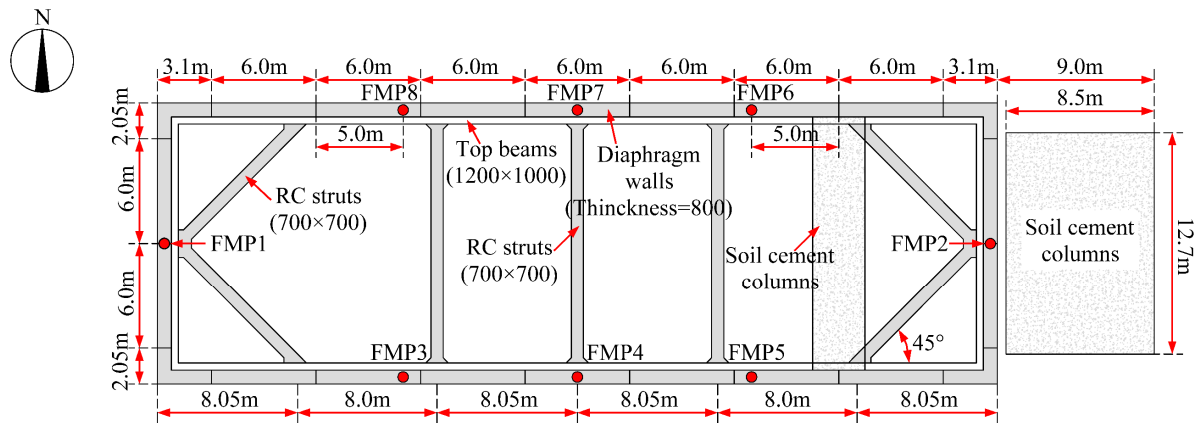
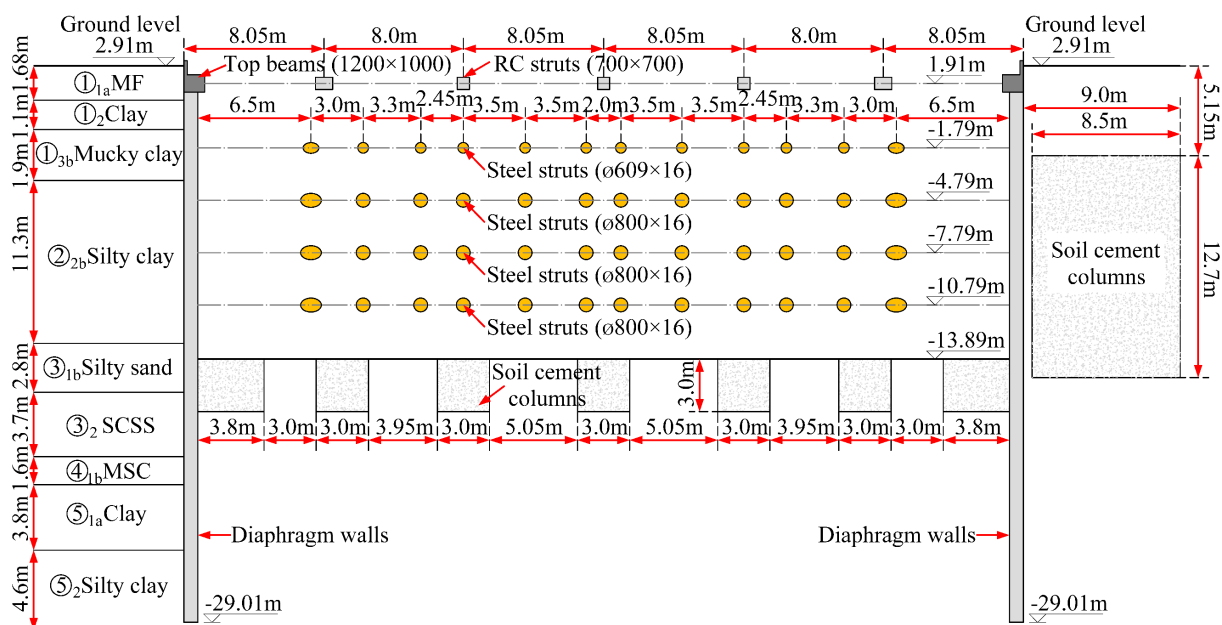


Figure 1. Planar layout of retaining structure for the excavation.



Note: MF=miscellaneous fill; MSC=mucky silty clay; SCSS=silty clay with silty sand.

Figure 2. Cross-sectional profile of retaining structure for the excavation.

3. Numerical Modelling

3.1. Numerical Model Size and Boundary Conditions

The commercial FE software PLAXIS 3D V20 was adopted in this paper, and the modelling dimensions were 55.79 m (depth along the z-axis), 200 m in the x-direction, and 150 m in the y-direction, which was sufficiently large to minimize the effect of boundary restraints [24,30,31]. The size of the numerical model and bracing system of the deep excavation are shown in Figure 3. The model was composed of 272,628 nodes and 167,118 elements.

In this study, the bottom boundary of the model was fixed vertically, while the top surface was left free. The lateral sides of the model were fixed in the horizontal direction, while vertical movement was allowed. The wall panels are modelled using isotropic plate elements, and the elastic properties of the concrete used to construct the wall are assumed to be $E = 31.5$ GPa, where E is Young's modulus, and $G = 13.13$ GPa, where G is the shear modulus. The value of the Poisson ratio is 0.2. The top beams and RC struts are modelled as linear elastic beam elements with a Young's modulus of $E = 31.5$ GPa, and the steel struts are modelled as linear elastic bar elements with Young's modulus of $E = 200$ GPa, which can transmit only axial force.

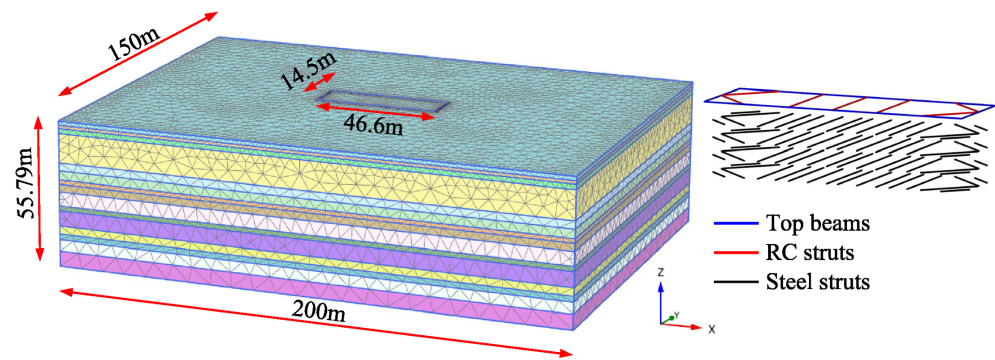


Figure 3. Modelling of the deep excavation and the bracing system.

3.2. Soil Constitutive Model and Input Parameters

An appropriate soil constitutive model and strength theory are important for the economic design of geotechnical structures [32], and numerous studies have verified that the deformation behavior of excavations can be more reasonably predicted using a hardening soil with a small-strain stiffness (HSS) model, which can appropriately consider the nonlinear and stress-dependent behavior of soils within a small range of strain, particularly in the soft ground along the southeast coastal areas of China [33–38].

There are 16 relevant parameters that should be input into the HSS model, and the basic parameters, namely, γ (i.e., unit weight), c' (i.e., effective cohesion), φ' (i.e., effective friction angle of soil), e (i.e., void ratio), and E_{s1-2} (i.e., Young's modulus at 1-D compression under the pressure of 100 kPa to 200 kPa), can be directly obtained via routine laboratory testing of soil samples, which is typically conducted during geological surveys. The remaining parameters, such as E_{oed}^{ref} , E_{50}^{ref} and E_{ur}^{ref} , which are time-consuming and costly to obtain via laboratory testing, are typically estimated from E_{s1-2} using certain proportionalities [18,24,37–42]. This paper mainly relies on the conclusions of Gu et al. [37] to estimate the remaining parameters due to the similarity between the geologies of the Ningbo and Shanghai areas. The values of the basic parameters are listed in Table 2, while the methods used to determine the values of the remaining parameters are summarised in Table 3.

Table 3. Values of the remaining HSS model parameters.

Parameters	Values
E_{oed}^{ref}	$E_{oed}^{ref} = 0.81E_{s1-2}$
ψ	Sand: $\psi = \varphi' - 30^\circ$, and when $\varphi' \leq 30^\circ$, $\psi = 0$; Clay: $\psi = 0$
R_f	$e > 1.5$, $R_f = 0.50$; $e < 1.0$, $R_f = 0.95$; $1.0 \leq e \leq 1.5$, $R_f = -0.9(e - 1.5) + 0.5$
E_{50}^{ref}	$E_{50}^{ref} = 1.02E_{s1-2}$
E_{ur}^{ref}	$E_{ur}^{ref} = 4.2E_{s1-2} + 7.25$
G_0^{ref}	Sand: $G_0^{ref} = 98.9e^{-0.45}$ MPa; Clay: $G_0^{ref} = 67.5e^{-1.57}$ MPa
p^{ref}	100 kPa
m	Sand: $m = 0.70$; Clay: $m = 0.65$
K_0	$K_0 = 1 - \sin\varphi'$
ν_{ur}	$\nu_{ur} = 0.2$
$\gamma_{0.7}$	$\gamma_{0.7} = 0.0001$

3.3. Excavation Sequence Simulation

The excavation was constructed using a cut-and-cover method, as shown in Figure 4, and was taken down in twelve stages, as detailed in Table 4. The dashed lines in Figure 4 represent the ground level at different stages of excavation, and the arrows represent struts. It should be noted that the field data were monitored after step 3 in practical construction processes. Therefore, the calculated deformations before step 4 were cleared to zero in the numerical analysis for the sake of comparison between field data and numerical results.

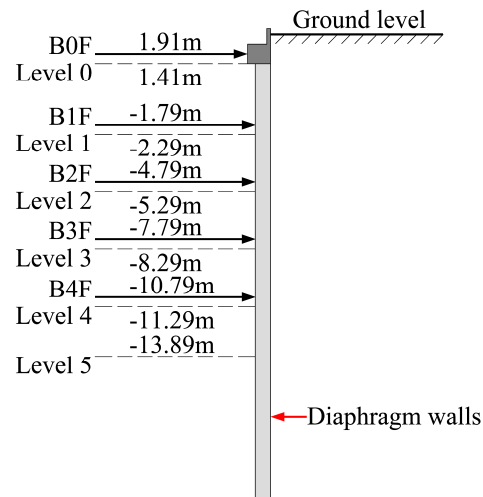


Figure 4. Excavation sequence.

Table 4. Stages of excavation in numerical analysis.

Stage	Description
1	Install diaphragm walls and soil cement columns.
2	Excavate to the level 1 at 1.41 m.
3	Install—1 level struts and top beams (B1F).
4	Excavate to the level 2 at—2.29 m.
5	Install—2 level struts (B2F).
6	Excavate to the level 3 at—5.29 m.
7	Install—3 level struts (B3F).
8	Excavate to the level 4 at—8.29 m.
9	Install—4 level struts (B4F).
10	Excavate to the level 5 at—11.29 m.
11	Install—5 level struts (B5F).
12	Excavate to the level 6 at—13.89 m.

3.4. Sensitive Analysis on the Mesh Size in Modelling

It is well established that, in theory, the greater the number of meshes in a finite element model and the finer the mesh division, the more accurate the calculated results will be. Nevertheless, an excessive number of meshes may also result in prolonged calculation times. In order to identify an optimal mesh size for the numerical model, five finite element models were constructed with varying mesh sizes, as illustrated in Table 5. The maximum calculated horizontal displacements of the diaphragm wall at the final stage of excavation in different meshing cases are presented in Figure 5.

Table 5. Meshing cases in sensitive analysis.

Meshing Cases	Average Mesh Size of Plate Elements (m)	Total Number of Elements and Nodes
Meshing 1	1.50	82,704 elements and 139,461 nodes
Meshing 2	1.25	126,565 elements and 211,775 nodes
Meshing 3	1.10	167,118 elements and 272,628 nodes
Meshing 4	0.95	240,874 elements and 386,024 nodes
Meshing 5	0.80	316,747 elements and 505,075 nodes

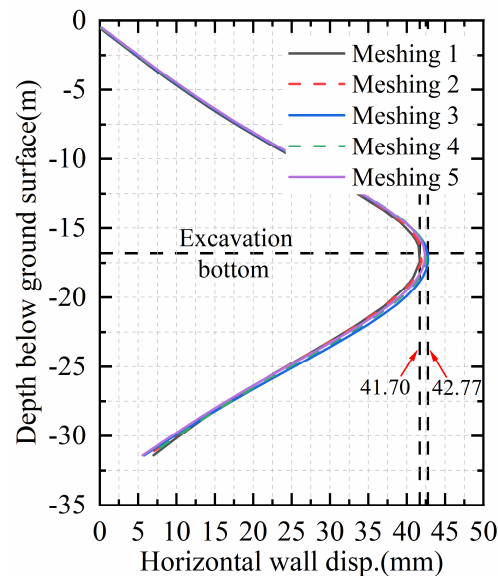


Figure 5. Horizontal wall displacements at the final stage of excavation in different meshing cases.

As shown in Figure 5, the calculated displacements of the five cases exhibit a high degree of similarity, with the largest discrepancy being only 1.07 mm. This is despite the fact that there is a difference of almost four times between the number of meshes with the highest and the number of meshes with the lowest number of meshes. It can be concluded that the calculated results are not sensitive to mesh size for the five meshing cases. After a detailed examination of the time required for model computation, it was determined that the meshing 3 would be the most suitable for use in subsequent analyses.

3.5. Modelling Method of Panel Joints

Little attention was previously paid to the effect of joints located between panels on the calculated displacements of diaphragm walls in small-scale deep excavation. In this study, locking pipe joints are used in the construction of diaphragm walls, and the geometry of diaphragm wall with a locking pipe joint is depicted in Figure 6. As shown in Figure 6, the locking pipe is installed at one end of the primary panel, and it will be moved to the end of the secondary panel after casting the concrete of the primary panel. The reinforcement cage of the secondary panel is then placed, the concrete of the secondary panel is cast, and so on until the end of the process. Compared to steel plate joints, locking pipe joints are widely used in practical applications due to their lower project cost and convenience. Generally, the locking pipe joint cannot sustain any significant out-of-plane bending moment about a vertical axis [25,27,28], and its function is similar to that of a hinge, which can only transmit axial and shear forces [43].

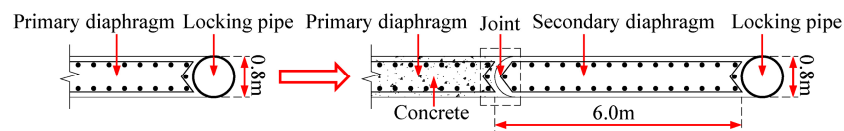


Figure 6. Planar layout of diaphragm wall joints.

As shown in Figure 7, the wall panels were modelled using isotropic plate elements, and a zone was created between the primary and secondary panels with a width equal to 0.5 times the diaphragm wall's thickness. The zone was modelled using cross-anisotropic plate elements and linear elastic bar elements, which were installed at intervals of 2 m along the vertical direction, and the interval between adjacent bar elements could be adjusted to the meshing dimensions.

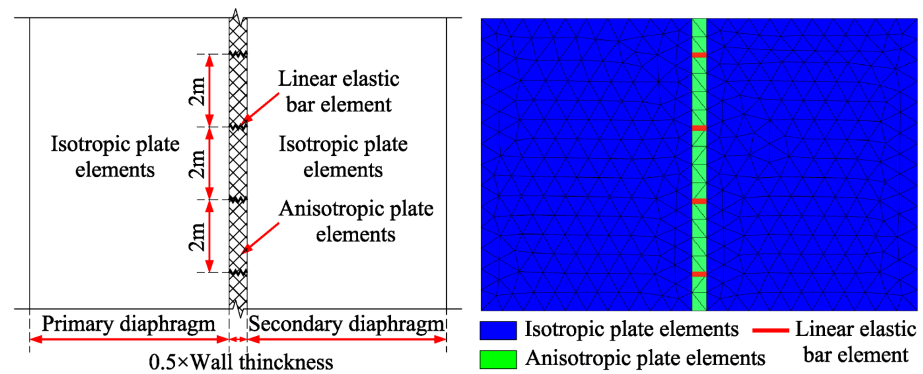


Figure 7. Elevation plan and meshing of the joint between wall panels.

As shown in Figure 8, bending moments and axial forces of an anisotropic plate can be expressed via Equations (1) and (2) [44,45]:

$$\begin{pmatrix} M_x \\ M_z \end{pmatrix} = \begin{pmatrix} \frac{E_x d^3}{12(1-\mu^2)} & \frac{\mu E_x d^3}{12(1-\mu^2)} \\ \frac{\mu E_z d^3}{12(1-\mu^2)} & \frac{E_z d^3}{12(1-\mu^2)} \end{pmatrix} \begin{pmatrix} \chi_x \\ \chi_z \end{pmatrix} \quad (1)$$

$$\begin{pmatrix} N_x \\ N_z \end{pmatrix} = \begin{pmatrix} E_x d & \mu E_x d \\ \mu E_z d & E_z d \end{pmatrix} \begin{pmatrix} \varepsilon_x \\ \varepsilon_z \end{pmatrix} \quad (2)$$

where M_x and M_z are the bending moments corresponding to rotation about the x-axis and z-axis, respectively; E_x and E_z are Young's modulus in the x and x directions, respectively; χ_x and χ_z are curvatures about the x-axis and z-axis, respectively; N_x and N_z are axial forces along the x-axis and z-axis, respectively; ε_x and ε_z are the axial strain values along the x-axis and z-axis, respectively; μ is the Poisson's ratio; and d is the thickness of plate.

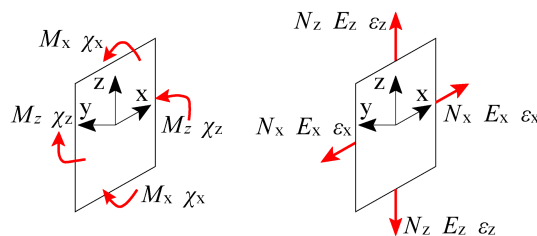


Figure 8. Bending moments and axial forces of an anisotropic plate.

This paper presents an adjustment to the E_x of anisotropic plate elements, modelling the joints to be close to zero (typically 10^{-6} GPa), while E_z is consistent with Young's modulus of isotropic plate elements for modelling the wall panels. Equation (1) suggests that as E_x approaches zero, M_x approaches zero, but N_x also approaches zero simultaneously, as expressed in Equation (2). This indicates that the horizontal axial force between adjacent wall panels cannot be adequately transmitted by the joint.

To address this issue, linear elastic bar elements, which could only transmit axial force, were installed at intervals of 2 m along the vertical direction between panels, and the Young's modulus of the bar elements was assumed to be $E_b = E \cdot d \cdot h$, where E is the Young's modulus of the concrete used to construct the wall, d is the thickness of the wall, and h specifies the intervals of the bar elements installed between panels. In that case, the axial stiffness of joints, characterised by E_b , and the bending stiffness of joints, characterised by E_x , could be specified independently to address weaknesses in each respective area, rather than being reduced equally [25,27,28]. In addition, the shear modulus of anisotropic plate elements was kept at the same level as that of isotropic plate elements, ensuring that the shear forces between adjacent wall panels could be adequately transmitted by the joint.

Using the above method, the function of the locking pipe joint could be approximated in terms of a hinge which could only transmit axial and shear forces via numerical analysis.

4. Results and Discussion

4.1. Influence of Joints between Wall Panels

As illustrated in Figure 1, eight field monitoring points (FMPs) were installed to monitor the horizontal displacement of the diaphragm walls during the excavation process using inclinometers. FMP1 and FMP2 were positioned at the midpoint of the short side, to the west and east of the excavation, respectively, while FMP3 and FMP7 were positioned at the midpoint of the long side, to the south and north of the excavation, respectively. The remaining FMPs were positioned approximately 3/10 of the distance from the end of the long side. Two numerical models were developed, and one consider the joints between panels using the proposed method, while the other disregard the joints conventionally. We compare the horizontal displacements of the walls, obtained by field monitoring, and two numerical models at all the FMPs at the final stage of excavation, as shown in Figure 9, and the magnitudes of the maximum wall displacements are summarised in Table 6. Due to the three-dimensional spatial effect, the deformation of the shorter side of the pit is significantly smaller than that of the longer side, which is consistent with the research of Ou et al. [7], Finno et al. [46] and Li et al. [47]. It should be noted that the calculated displacements at FMP3 and FMP8 are indistinguishable due to the symmetry on the x-axis of the numerical model, as depicted in Figure 1; therefore, their calculated displacements are plotted on the same graph. The same applies to points FMP4 and FMP7, as well as to points FMP5 and FMP6.

As shown in Figure 9a,b, for FMPs located on the short side, there is a significant difference between the calculated displacements obtained by the two methods, and a better agreement was found between the monitored and calculated displacements when considering the joints compared to disregarding them, indicating the effectiveness of the proposed method. Table 6 demonstrates a significant reduction in the error of the calculated displacements when the joints are considered as proposed, and the average error of the calculated displacements considering the joints is only 8.76%, while it reaches an average error of 66.91% when the joints are disregarded as is conventional. This leads to the conclusion that the joints between the wall panels have a significant influence on the calculated displacements of the short side in the investigated excavation. The significant difference is primarily attributed to the influence in the excavation corner effect. When the joints are disregarded, the diaphragm wall in short side is regarded as an integrated whole, and the bending deformation of the short side in the horizontal direction is more constrained by the excavation corner. This results in a considerable horizontal stiffness of the diaphragm wall in the short side, which will result in a restriction of the deformation of the diaphragm wall. Consequently, the calculated displacement under earth pressure is minimal, resulting in significant error. However, when the joints are considered, their functions are similar to those of a hinge [43], and the bending deformation of the short side in the horizontal direction is less constrained, resulting in relatively larger deformation and small errors.

As shown in Figure 9c–e, the calculated displacements of the two numerical models are very similar for the FMPs located on the long side, and even approximately the same for FMP4 and FMP7. The monitored and calculated horizontal displacements show a reasonable agreement, which also demonstrates the validity of the numerical models. Table 6 shows that the average error of the maximum calculated displacements is 13.88% and 16.03% for the numerical model when considering and disregarding joints, respectively. The observations suggest that placing joints between the wall panels has a slight influence on the calculated displacements of the long side in the investigated excavation, and the relative error of the maximum calculated displacements of the FMPs is slightly smaller when considering the joints compared to disregarding them. This is consistent with the results of Dong et al. [25], who investigated a high-rise building excavation and concluded

that the deformations at the midpoint of a stretch of wall are not sensitive to the anisotropy factor that reflects joint weakness. The difference between the calculated displacements obtained using the two methods is minimal, and it is primarily attributable to the fact that the FMPs of the long side are situated at a considerable distance from the excavation corner. As the distance from the corner increases, the bending deformation of the diaphragm wall in the horizontal direction is less constrained by the excavation corner. Even in the absence of the consideration of the joints, the horizontal stiffness of the diaphragm wall, which is regarded as an integrated whole, is already modest, and the deformation of the diaphragm wall is predominantly influenced by its vertical stiffness and by the struts stiffness. When the excavation is sufficiently long, the plane strain ratio (PSR), which refers to the ratio of the displacement of the wall under 3D simulation conditions to the displacement of the wall under the 2D plane strain condition, is close to 1.00 [7,47]. It is widely acknowledged that the horizontal stiffness of the diaphragm wall is not accounted for in the 2D numerical model. When the plane strain ratio (PSR) is equal to 1.00, it can be understood that the horizontal stiffness of the diaphragm wall in the 3D numerical model has no impact on the deformation of the excavation. As illustrated in Figure 9e, the calculated displacements of FMP4 and FMP7 derived from the 3D model are found to be in close agreement with those obtained from the 2D model. This indicates that the plane strain ratio (PSR) is close to 1.00, and the horizontal stiffness of the diaphragm wall on the long side, which is influenced by the joints between wall panels, exerts a minimal influence on its deformation.

Table 6. Comparison of monitored and calculated maximum displacements at FMPs.

Site	Max. Monitored Disp. (mm)	Max. Calculated Disp. (mm)		Relative Error	
		Proposed	Conventional	Proposed	Conventional
FMP1	19.72	19.98	6.37	1.34%	67.68%
FMP2	16.57	13.89	5.61	16.17%	66.14%
Short side			average	8.76%	66.91%
FMP3	43.62	38.66	37.15	11.37%	14.83%
FMP4	46.04	42.87	42.77	6.89%	7.10%
FMP5	44.82	38.59	37.23	13.90%	16.93%
FMP6	51.63	38.59	37.23	25.26%	27.89%
FMP7	49.37	42.87	42.77	13.17%	13.37%
FMP8	44.27	38.66	37.15	12.67%	16.08%
Long side			average	13.88%	16.03%

The maximum horizontal displacements of the walls obtained by monitoring and two numerical methods at each excavation stage are shown in Figure 10, and a similar conclusion can be drawn. For the short side, the joints have a significant influence on the calculated displacements at each excavation stage, and the calculated displacements obtained by the proposed method are much closer to the monitored displacements compared to those obtained by the conventional method. For the long side, the calculated displacements obtained by the two methods at every stage are similar. This confirms that the influence of the joints on the calculated displacements at each excavation stage is relatively slight. However, the calculated displacements that take the joints into consideration as proposed are slightly closer to the monitored displacements at each stage.

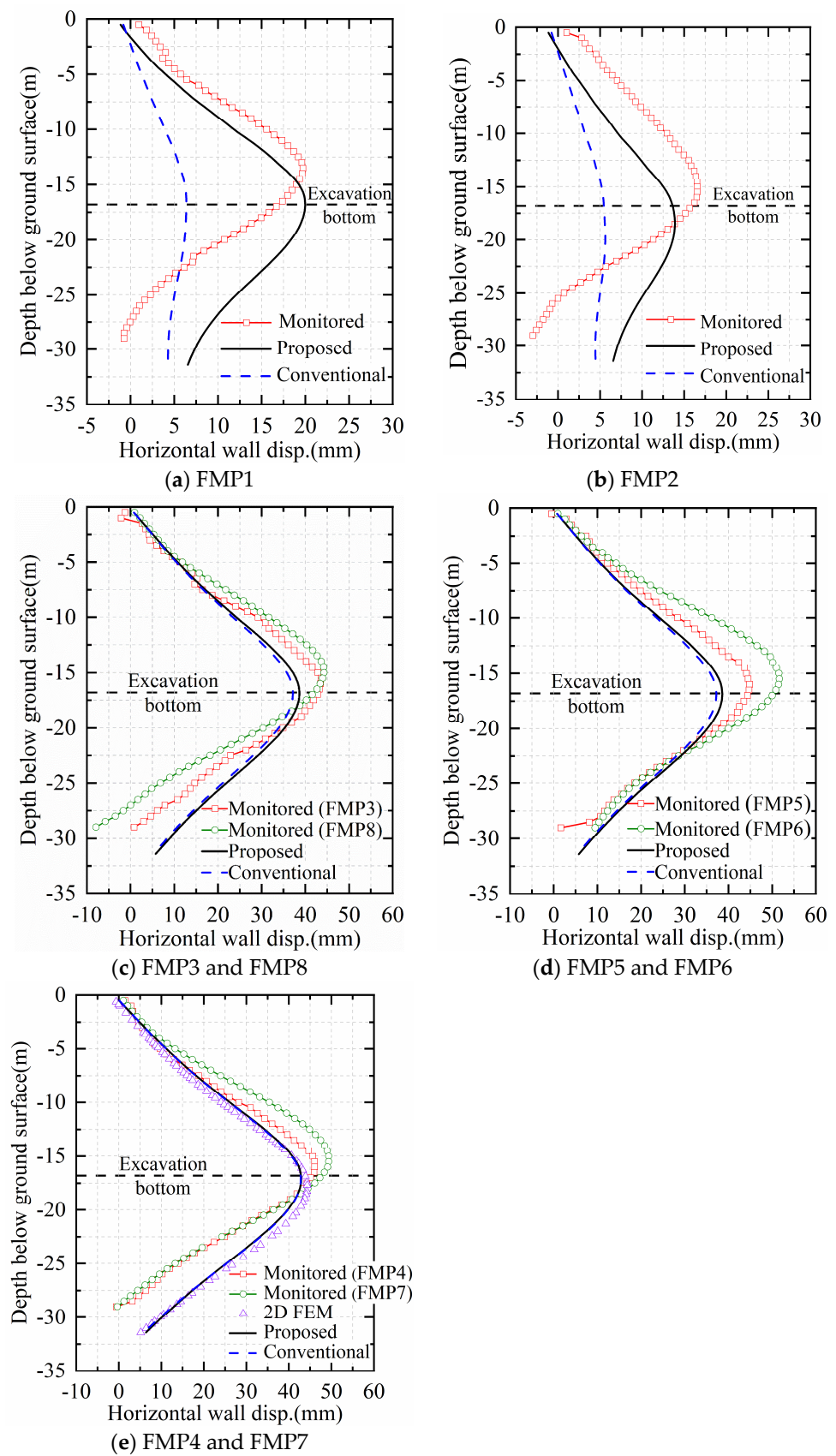


Figure 9. Horizontal wall displacements at the final stage of excavation, assessed by field monitoring; proposed numerical method, considering joints; and conventional numerical method, disregarding joints.

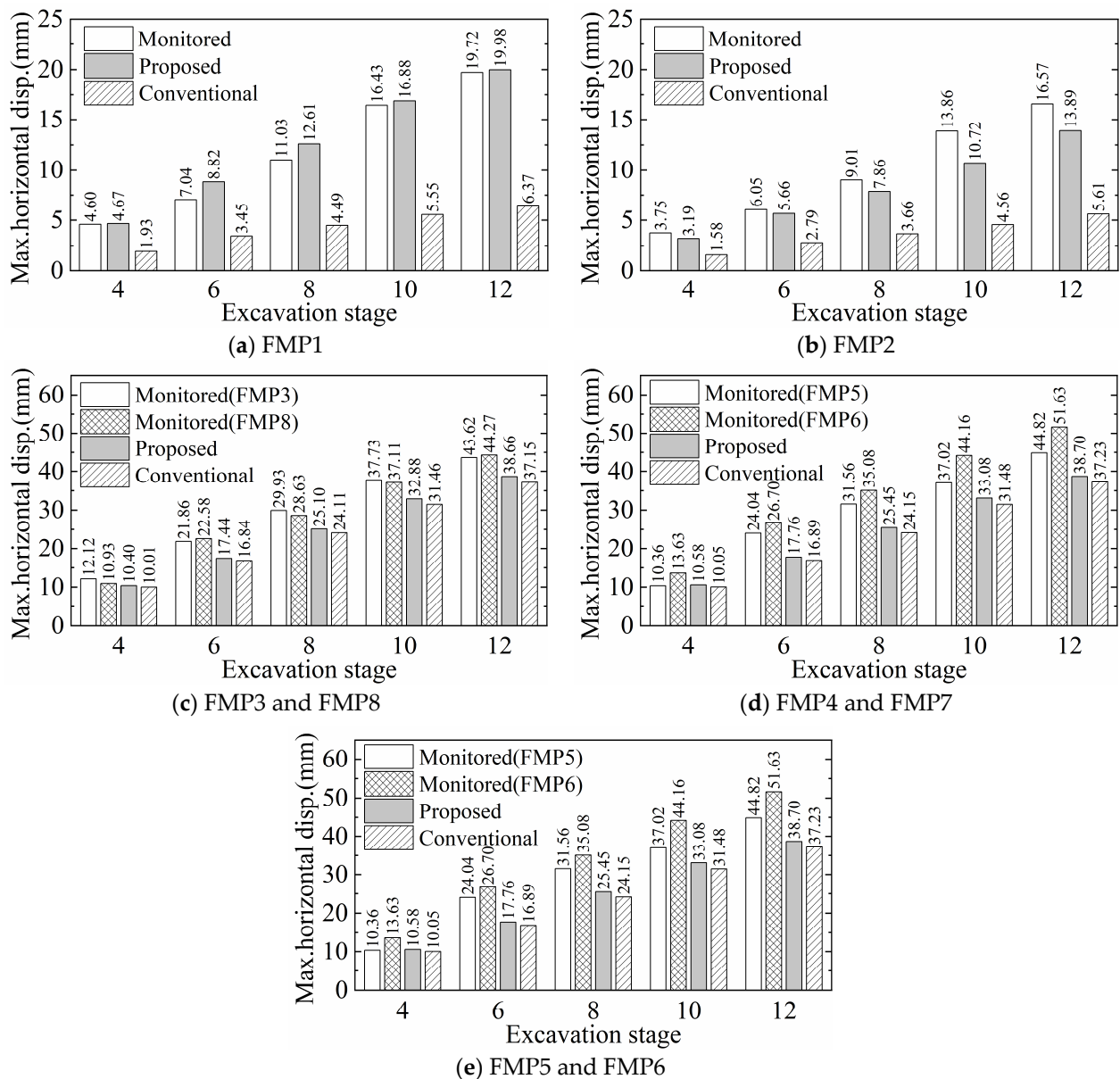


Figure 10. Maximum horizontal displacements at each excavation stage, assessed by field monitoring; proposed numerical method, considering joints; and conventional numerical method, disregarding joints.

The horizontal displacements of the walls, obtained by monitoring, and two numerical methods at the depth of the excavation bottom are compared, as shown in Figure 11. The comparisons also indicate that the numerical model considering joints with the proposed method provides a better fit to the monitored data. The calculated displacements of the wall, determined by considering the joints at the depth of the excavation bottom, exhibit a broken-line deformation mode, the deformation of each individual panel displays an approximately linear pattern, and there is a significant turning point between panels. This indicates that the bending deformation of each individual panel in the horizontal direction is small, adjacent panels turn at the position of the joints, and this is consistent with the phenomenon where cracking and leakage often occur at the joints between panels during the excavation process (as shown in Figure 12) [48–52]. It should be noted, however, that the leakage is relatively slow and small, and therefore not included in the modelling. As shown in Figure 11c, the gradient of the broken line is higher in the initial two joints at the head and tail ends of the long side, decreasing towards the center. As shown in Figure 11a,b,

the broken line within the initial joint of the short side exhibits an aberrant negative value, indicating that the walls installed at the end of the short side are deformed outwards by the excavation. This is likely to be caused by the rotation of the L-type wall installed at the corner of the excavation, which is induced by the overall deformation of the long side of the diaphragm walls and the earth pressure difference between the longer and shorter sections of the L-type wall, as shown in Figure 13.

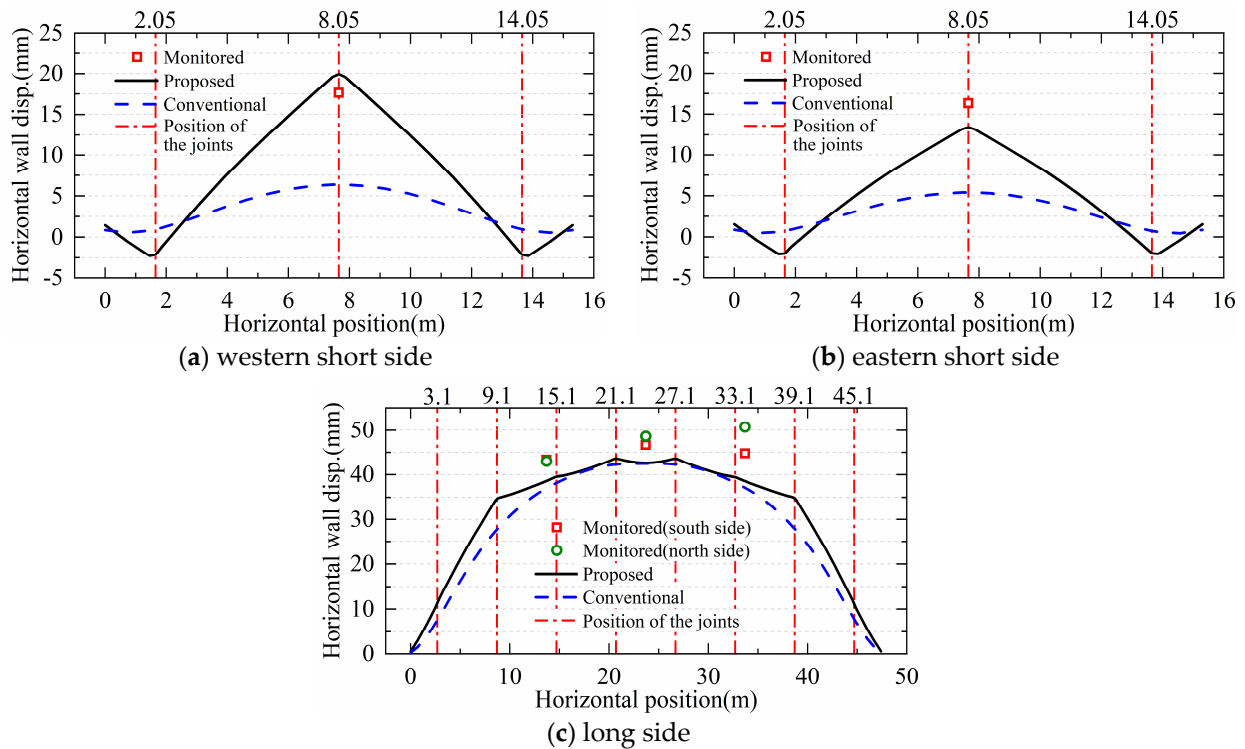


Figure 11. Horizontal wall displacements at the excavation bottom, assessed by field monitoring; proposed numerical method, considering joints; and conventional numerical method, disregarding joints.

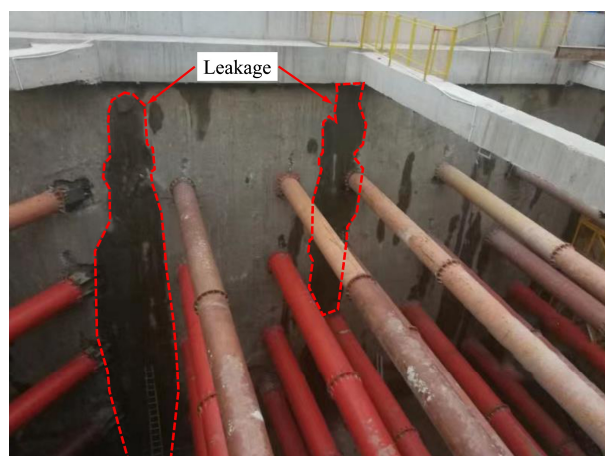


Figure 12. Leakage occurred at the joints between panels in this study.

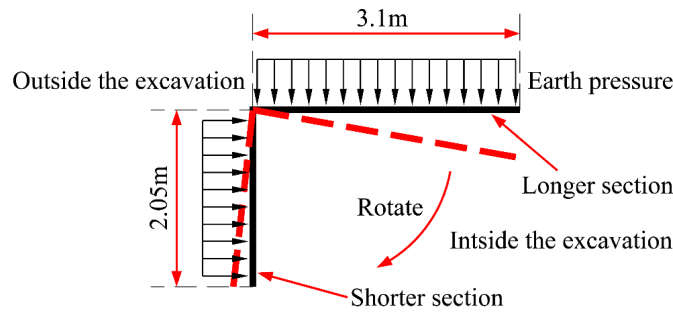


Figure 13. Deformation of L-type diaphragm wall at the corner.

By contrast, the calculated displacements of the wall, disregarding the joints at the depth of excavation’s bottom, exhibit a smooth curve deformation mode, and the curve of the long side is close to the broken line aforementioned, while there is a clear difference between the curve and broken line of the short side, obtained by the two numerical models, respectively.

Figure 14 shows the contours of bending moments of the z-axis of the wall panel, located at the center of the long side of the excavation. This panel was selected for exhibition as its deformation was typically the largest. As shown in Figure 14a, the bending moments of the z-axis around the steel struts obtained by the proposed method are extremely large, while they are very small in the remaining zone, which coincides with the actual reinforcement of the diaphragm walls. In practical applications, horizontal reinforcement is typically concentrated near the steel structures to sustain the strut forces, with sparse reinforcement located elsewhere that only meets the construction demand [53]. Additionally, the bending moments of the z-axis of the joints are close to zero, which coincides with the function of the joints. In contrast, as shown in Figure 14b, significant bending moments of the z-axis, obtained by the conventional method, are observed at the zone near the excavation bottom and in the zone around the steel structures. The calculated maximum bending moments of the z-axis of the wall panel and the joints reach almost 480 kN·m/m, indicating that substantial reinforcement in the horizontal direction of wall panels and joints would be required, which is not typically carried out in practice.

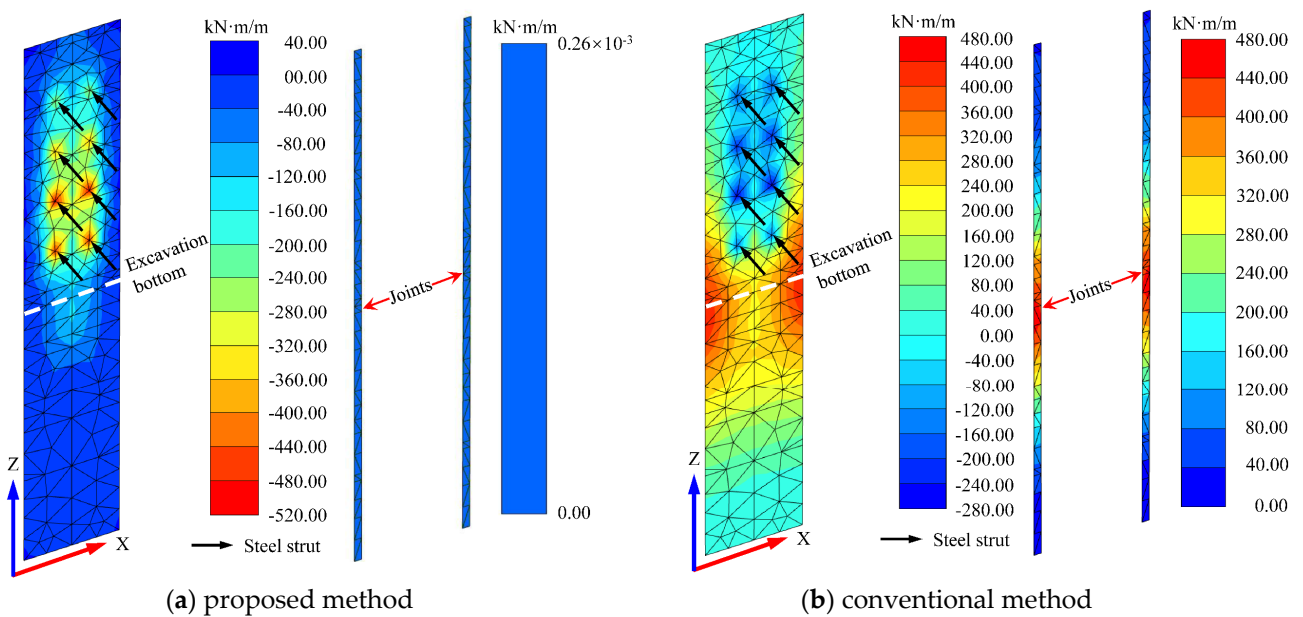


Figure 14. Contours of bending moments about the z-axis of the wall panel by as determined by (a) the proposed numerical method considering joints; and (b) the conventional numerical method, disregarding joints.

In summary, the proposed method for modelling the joints with anisotropic plate elements and elastic bar elements was validated via a comparison with the results of field monitoring. The calculated results when considering the joints are more consistent with the actual deformation and force behavior of diaphragm walls, and calculation disregarding the joints may cause the calculated displacements to be underestimated and the bending moments about a horizontal axis to be overestimated. Moreover, the joints between the wall panels have a significant influence on the calculated displacements for the short side, while it is relatively slight for the long side. In comparison to the method used by Zdravkovic et al. [26] and Dong et al. [25,27,28], the method proposed in this paper does not necessitate trial-and-error or back analysis based on actual monitored data in order to determine the reduced ratio, which renders it more convenient for application in practical engineering. However, the calculated displacements at the toe of diaphragm walls are typically greater than the monitored values, which is consistent with the results of Gu et al. [37] and deserves further investigation.

4.2. Influence of the Excavation Length

The analyses in the previous section indicate that placing joints between panels has two distinct effects on the calculated displacements. These are specific to the long side and short side, respectively, in an identical numerical model. To investigate the influence of the excavation length on the relative difference between the calculated displacements obtained by the two methods, six additional operating cases were analysed, as shown in Figure 15, and each case also included two numerical models: one model considered the joints as proposed, while the other considered it conventionally. The modelling procedures in the subsequent analysis were the same as those used in the previous analysis, except for the variation in excavation length.

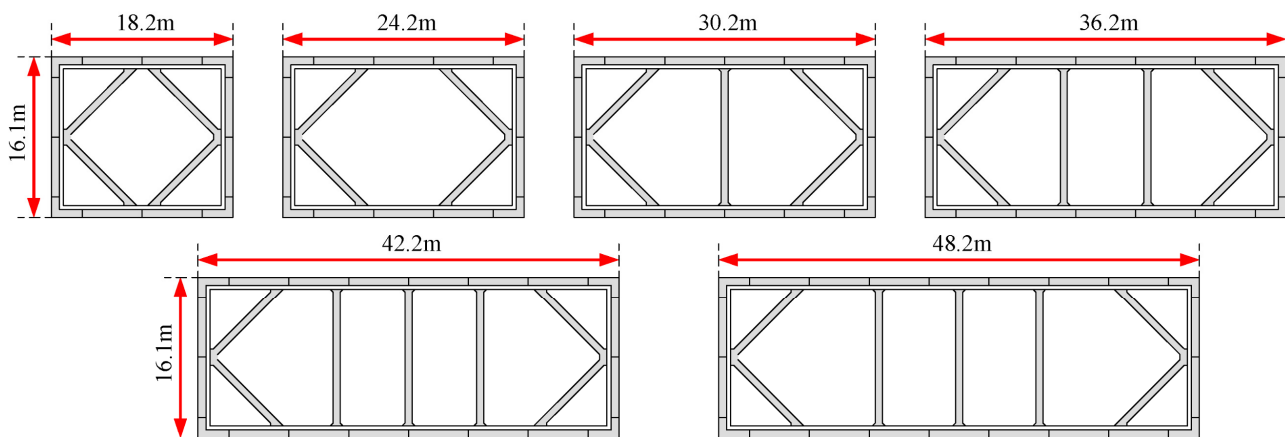


Figure 15. Planar layout of excavation with different length.

Figure 16 presents the calculated displacements that occurred at the center of the excavation length for the six cases, while Figure 17 illustrates the differences between the maximum calculated displacements obtained by the two methods used for the six cases. The relative differences in Figure 17 and in the following sections are defined as shown in Equation (3).

$$D = \frac{y_{\max}^p - y_{\max}^c}{y_{\max}^p} \times 100\% \quad (3)$$

where y_{\max}^p is the maximum calculated displacements obtained by the proposed method, and y_{\max}^c is the maximum calculated displacements obtained via the conventional method.

It was found that when the excavation length was 18.2 m (as shown in Figure 16a), the maximum calculated displacement obtained via the conventional method was 15.36 mm, while the value obtained by the proposed method was 29.82 mm. There was a significant difference of almost 50% between the calculated displacements derived from the two methods (as shown in Figure 17). The significant differences could be attributed primarily to the reduction in the horizontal stiffness of the diaphragm wall, caused by the use of joints in the proposed method, which had a significant influence on the deformation of the excavation with small plan dimensions. As the excavation length increased, the displacement curves obtained by the two methods gradually became closer (as shown in Figure 16), and the difference between them decreased (as shown in Figure 17). At a length of 48.2 m, the maximum calculated displacements obtained by the conventional method was 42.77 mm, while the value obtained by the proposed method was 42.87 mm, and the two curves almost coincided, as shown in Figure 16f. The difference between these values was almost zero, as shown in Figure 17. This was primarily due to the excavation length becoming longer, which in turn reduced the horizontal stiffness of the diaphragm wall. When the excavation was sufficiently long, the deformation of the diaphragm wall was predominantly influenced by its vertical stiffness and the struts stiffness, and the horizontal stiffness of the diaphragm wall had a negligible effect on its deformation. Consequently, the joints, which affected the horizontal stiffness, had a minimal influence on the calculated displacements, and the difference between the maximum calculated displacements obtained by two models was also small. The results indicate that the excavation length is negatively correlated with the relative difference between the calculated displacements obtained by the two methods. In other words, the shorter the excavation, the greater the influence of the joints have on the calculated displacement, and the more necessary it is to take them into account in the numerical models.

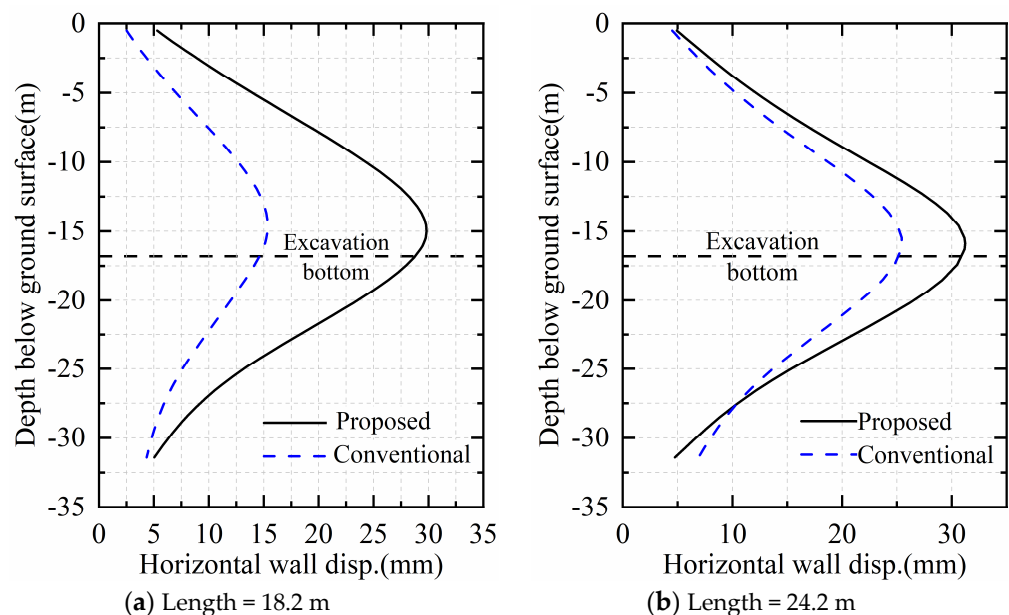


Figure 16. Cont.

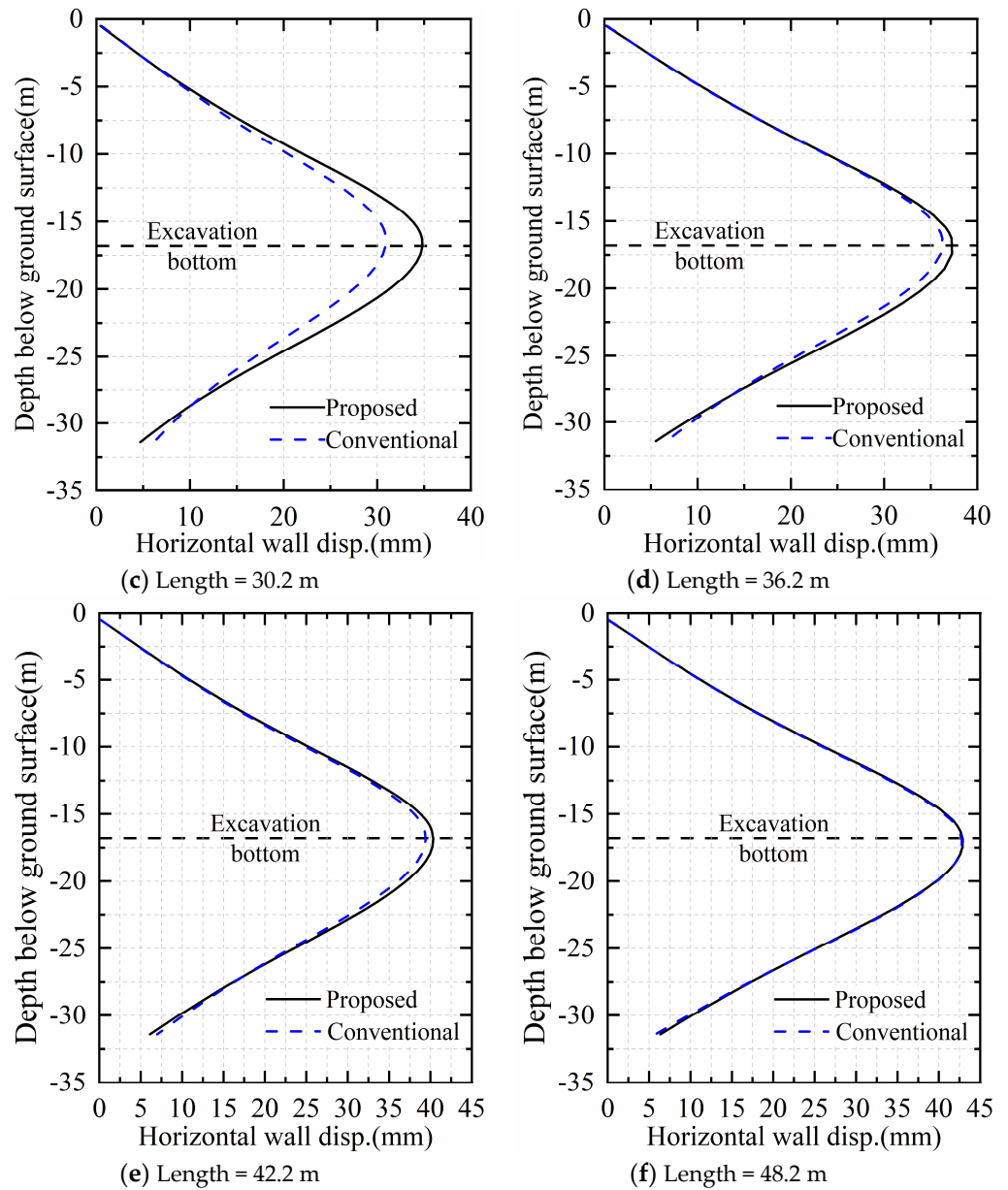


Figure 16. Horizontal wall displacements at the final stage by proposed numerical method considering joints and conventional numerical method disregarding joints for different excavation lengths.

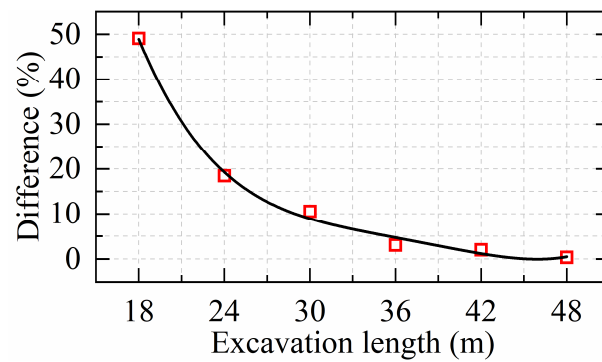


Figure 17. Differences between the calculated displacements obtained by the two methods for various excavation lengths.

4.3. Influence of the Excavation Depth and Diaphragm Wall Thickness

A similar series of analyses was carried out to investigate the influence of the excavation depth and diaphragm wall thickness on the difference between the calculated displacements obtained by the two methods. In practical applications, diaphragm walls are commonly constructed with thicknesses of 0.6, 0.8, 1.0, and 1.2 m [41,53], and it should be noted that each diaphragm wall thickness is suitable for a particular range of excavation depths. For example, diaphragm walls with a thickness of 1.2 m are typically used to brace an excavation with a depth of 30.0 to 40.0 m. In this paper, three operating cases with different excavation depths were analysed for each diaphragm wall thickness, as illustrated in Table 7, and each case also included two numerical models.

Table 7. Calculation cases.

Operating Cases	Excavation Depth (m)	Diaphragm Wall Thickness (m)
Case 1	10.8	0.6
Case 2	16.8	
Case 3	22.8	
Case 4	16.8	0.8
Case 5	22.8	
Case 6	28.8	
Case 7	22.8	1.0
Case 8	28.8	
Case 9	34.8	
Case 10	28.8	1.2
Case 11	34.8	
Case 12	40.8	

The excavation length for the twelve cases was set to be 30.0 m, and one strut level was added or removed for every 3.0 m change in excavation depth based on previous numerical models with excavation depths of 16.8 m. The differences between the maximum calculated displacements obtained by the two methods are depicted in Figures 18 and 19 for different excavation depths and different diaphragm wall thicknesses, respectively, where T and H are diaphragm wall thickness and excavation depth, respectively.

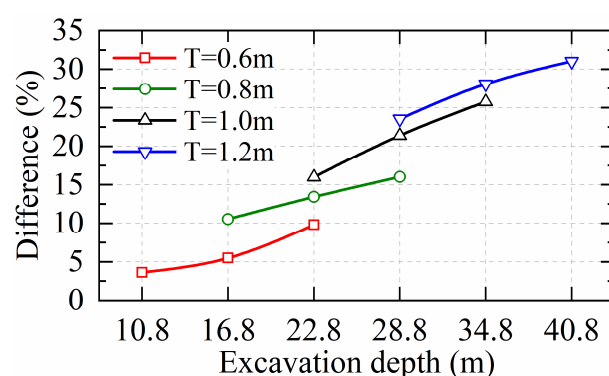


Figure 18. Differences between the calculated displacements obtained by the two methods for different excavation depths.

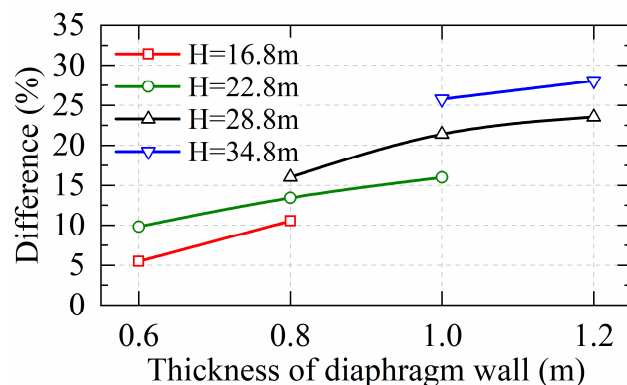


Figure 19. Differences between the calculated displacements obtained by the two methods for different diaphragm wall thicknesses.

As shown in Figure 18, the relative error increases with the thickness of the diaphragm wall for the same excavation depth. It can also be observed from Figure 19 that the differences increase with the diaphragm wall thickness for cases with the same excavation depth. To summarise, there is a positive correlation between the excavation depth and diaphragm wall thickness with the difference in calculated displacements obtained by the two methods. Therefore, we recommend considering the joints in diaphragm wall modelling for small-scale deep excavations, particularly for deeper excavations or thicker diaphragm walls.

5. Conclusions

This current paper proposed a new method for modelling joints between panels using anisotropic plate elements and elastic bar elements and then analysed the displacements of diaphragm walls in a small-scale deep excavation considering joints. The general conclusions from the study are summarised below.

- (1) The proposed method for modelling the joints was validated by yielding horizontal displacements in diaphragm walls that more closely matched the results of the field monitoring.
- (2) For small-scale deep excavations, the calculated results, which take into account the joints, are more accurate in predicting the deformation and force behaviour of diaphragm walls. Disregarding the joints may result in an underestimation of the calculated displacements and an overestimation of bending moments about a vertical axis.
- (3) The joints between the wall panels have a significant influence on the calculated displacements for the short side of the excavation investigated, while the influence is relatively slight for the long side of the excavation investigated.
- (4) For small-scale deep excavations, the influence of the joints on the calculated displacement is greater when the excavation is shorter and deeper, or when the diaphragm wall is thicker. Therefore, it is necessary to take this factor into account in the numerical models when dealing with the aforementioned situations.

Author Contributions: Conceptualization, M.Y. and C.T.; Data curation, M.Y.; Formal analysis, M.Y. and B.T.; Funding acquisition, R.W.; Investigation, J.C.; Methodology, M.Y. and C.T.; Project administration, R.W.; Resources, J.C.; Software, B.T.; Validation, J.C.; Writing—original draft, M.Y.; Writing—review & editing, R.W. and C.T. All authors have read and agreed to the published version of the manuscript.

Funding: This research was funded by the Ningbo Commonweal Research Program, grant number 2023S131, and Zhejiang Construction Scientific Research Program, grant number 2021K133.

Data Availability Statement: The data used to support the findings of this study are available from the corresponding author upon request.

Acknowledgments: The authors appreciate the anonymous reviewers for their constructive comments and suggestions that significantly improved the quality of this manuscript.

Conflicts of Interest: Author Jianwei Chen was employed by the company Ningbo Urban Construction Design & Research Institute Co., Ltd. Author Bing Tang was employed by the company China Railway Siyuan Survey and Design Group Co., Ltd. The remaining authors declare that the research was conducted in the absence of any commercial or financial relationships that could be construed as a potential conflict of interest.

Abbreviations

Notation

E	Young's modulus of concrete or steel
G	Shear modulus of concrete
γ	Unit weight of soil
c'	Effective cohesion of soil
φ'	Effective friction angle of soil
e	Void ratio of soil
E_{s1-2}	Young's modulus of soil at 1-D compression under the pressure of 100 kPa to 200 kPa
R_{inter}	Interface strength reduction between structure and soil
E_{oed}^{ref}	Young's modulus at 1-D compression at the reference mean pressure, p^{ref}
E_{50}^{ref}	Young's modulus at 50% shear strength at the reference mean pressure, p^{ref}
E_{ur}^{ref}	Unload–reload Young's modulus at the reference mean pressure, p^{ref}
ψ	Angle of dilation
R_f	Failure ratio
G_0^{ref}	Very small strain shear modulus at the reference mean pressure, p^{ref}
p^{ref}	Reference mean pressure
m	Power in stiffness power laws
K_0	Coefficient of earth pressure at rest
ν_{ur}	Unload–reload Poisson's ratio
$\gamma_{0.7}$	Threshold strain
M_x	Bending moments corresponding to rotation about the x-axis
M_z	Bending moments corresponding to rotation about the z-axis
E_x	Young's modulus in the X directions
E_z	Young's modulus in the Z directions
μ	Poisson's ratio
d	Thickness of plate
χ_x	Curvatures about the x-axis
χ_z	Curvatures about the z-axis
N_x	Axial force along the x-axis
N_z	Axial force along the z-axis
ε_x	Axial strain along the x-axis
ε_z	Axial strain along the z-axis
E_b	Young's modulus of the bar elements
y_{max}^p	The maximum calculated displacements obtained by the proposed method
y_{max}^c	The maximum calculated displacements obtained by conventional method

References

- Comodromos, E.M.; Papadopoulou, M.C.; Konstantinidis, G.K. Effects from diaphragm wall installation to surrounding soil and adjacent buildings. *Comput. Geotech.* **2013**, *53*, 106–121. [[CrossRef](#)]
- Spruit, R.; van Tol, F.; Broere, W.; Doornenbal, P.; Hopman, V. Distributed temperature sensing applied during diaphragm wall construction. *Can. Geotech. J.* **2017**, *54*, 219–233. [[CrossRef](#)]
- Spruit, R.; van Tol, F.; Broere, W.; Slob, E.; Niederleithinger, E. Detection of anomalies in diaphragm walls with crosshole sonic logging. *Can. Geotech. J.* **2014**, *51*, 369–380. [[CrossRef](#)]
- Kim, D.K. Seismic response analysis of reinforced concrete wall structure using macro model. *Int. J. Concr. Struct. Mater.* **2016**, *10*, 99–112. [[CrossRef](#)]
- Houhou, M.N.; Emeriault, F.; Belouar, A. Three-dimensional numerical back-analysis of a monitored deep excavation retained by strutted diaphragm walls. *Tunneling Undergr. Space Technol.* **2019**, *83*, 153–164. [[CrossRef](#)]

6. Liu, N.; Pan, J.; Li, M.; Li, Y. Deformation characteristics of an ultra-deep and small-scale rectangular excavation in Hangzhou soft clay. *Tunneling Undergr. Space Technol.* **2023**, *137*, 105117. [[CrossRef](#)]
7. Ou, C.Y.; Chiou, D.C.; Wu, T.S. Three-dimensional finite element analysis of deep excavations. *J. Geotech. Eng.* **1996**, *122*, 337–345. [[CrossRef](#)]
8. Kim, D.S.; Lee, B.C. Instrumentation and numerical analysis of cylindrical diaphragm wall movement during deep excavation at coastal area. *Mar. Georesour. Geotechnol.* **2005**, *23*, 117–136. [[CrossRef](#)]
9. Liu, G.B.; Jiang, R.J.; Ng, C.W.; Hong, Y. Deformation characteristics of a 38 m deep excavation in soft clay. *Can. Geotech. J.* **2011**, *48*, 1817–1828. [[CrossRef](#)]
10. Zhang, R.; Wu, C.; Goh, A.T.; Böhlke, T.; Zhang, W. Estimation of diaphragm wall deflections for deep braced excavation in anisotropic clays using ensemble learning. *Geosci. Front.* **2021**, *12*, 365–373. [[CrossRef](#)]
11. Zhang, D. Influences of Deep Foundation Pit Excavation on the Stability of Adjacent Ancient Buildings. *Buildings* **2023**, *13*, 2004. [[CrossRef](#)]
12. GB 50497-2019; Technical Standard for Monitoring of Building Excavation Engineering. China Planning Press: Beijing, China, 2012; pp. 34–35.
13. DG/TJ 08-2001-2016; Specification for Foundation Excavation Monitoring. Tongji University Press: Shanghai, China, 2016; p. 42.
14. Su, Y.; Wang, J.; Li, D.; Wang, X.; Hu, L.; Yao, Y.; Kang, Y. End-to-end deep learning model for underground utilities localization using GPR. *Automat. Constr.* **2023**, *149*, 104776. [[CrossRef](#)]
15. Lei, J.; Fang, H.; Zhu, Y.; Chen, Z.; Wang, X.; Xue, B.; Wang, N. GPR detection localization of underground structures based on deep learning reverse time migration. *NDTE Int.* **2024**, *143*, 103043. [[CrossRef](#)]
16. Hou, Y.M.; Wang, J.H.; Zhang, L.L. Finite-element modeling of a complex deep excavation in Shanghai. *Acta. Geotech.* **2009**, *4*, 7–16. [[CrossRef](#)]
17. Nogueira CD, L.; Azevedo RF, D.; Zornberg, J.G. Validation of coupled simulation of excavations in saturated clay: Camboinhas case history. *Int. J. Geomech.* **2011**, *11*, 202–210. [[CrossRef](#)]
18. Hsiung BC, B.; Yang, K.H.; Aila, W.; Ge, L. Evaluation of the wall deflections of a deep excavation in Central Jakarta using three-dimensional modeling. *Tunneling Undergr. Space Technol.* **2018**, *72*, 84–96. [[CrossRef](#)]
19. Di Mariano, A.; Amoroso, S.; Arroyo, M.; Monaco, P.; Gens, A. SDMT-based numerical analyses of deep excavation in soft soil. *J. Geotech. Geoenviron.* **2019**, *145*, 04018102. [[CrossRef](#)]
20. Xie, C.Y.; Nguyen, H.; Choi, Y.; Armaghani, D.J. Optimized functional linked neural network for predicting diaphragm wall deflection induced by braced excavations in clays. *Geosci. Front.* **2022**, *13*, 101313. [[CrossRef](#)]
21. Guo, P.; Gong, X.; Wang, Y. Displacement and force analyses of braced structure of deep excavation considering unsymmetrical surcharge effect. *Comput. Geotech.* **2019**, *113*, 103102. [[CrossRef](#)]
22. Schwamb, T.; Soga, K. Numerical modelling of a deep circular excavation at Abbey Mills in London. *Géotechnique* **2015**, *65*, 604–619. [[CrossRef](#)]
23. Pedro, A.; Zdravković, L.; Potts, D.; Almeida e Sousa, J. Numerical modelling of the Ivens shaft construction in Lisbon, Portugal. *Proc. Inst. Civil. Eng. Geotech.* **2019**, *172*, 263–282. [[CrossRef](#)]
24. Chu, Y.D.; Chen, W.Z.; Tian, H.M.; Cao, J.J.; Geng, Y.M.; Chen, P.S. Stability analysis of large shield working well considering effect of diaphragm wall joint. *Rock Soil Mech.* **2011**, *32*, 2937–2950.
25. Dong, Y.P.; Burd, H.J.; Houlsby, G.T. Finite-element analysis of a deep excavation case history. *Géotechnique* **2016**, *66*, 1–5. [[CrossRef](#)]
26. Zdravkovic, L.; Potts, D.M.; St John, H.D. Modelling of a 3D excavation in finite element analysis. *Géotechnique* **2005**, *55*, 497–513. [[CrossRef](#)]
27. Dong, Y.; Burd, H.; Houlsby, G.; Hou, Y. Advanced finite element analysis of a complex deep excavation case history in Shanghai. *Front. Struct. Civ. Eng.* **2014**, *8*, 93–100. [[CrossRef](#)]
28. Dong, Y.P.; Burd, H.J.; Houlsby, G.T. Finite element parametric study of the performance of a deep excavation. *Soils. Found.* **2018**, *58*, 729–743. [[CrossRef](#)]
29. Chen, J.J.; Wang, J.H.; Qiao, P.; Hou, Y.M.; Gu, Q.Y. Shear bearing of cross-plate joints between diaphragm wall panels—II, numerical analysis and prediction formula. *Mag. Concrete Res.* **2016**, *68*, 1025–1039. [[CrossRef](#)]
30. Yi, L.J.; Li, Y.J.; Zhu, Y.P.; Huo, B.; Yang, Z.T.; Duan, Q.C. Monitoring and numerical simulation of support for foundation pit at Yanyuan Road Station of Lanzhou Metro. *Chin. J. Geotech. Eng.* **2021**, *43*, 111–116.
31. Hsieh, P.G.; Ou, C.Y. Shape of ground surface settlement profiles caused by excavation. *Can. Geotech. J.* **1998**, *35*, 1004–1017. [[CrossRef](#)]
32. Lu, D.; Ma, C.; Du, X.; Jin, L.; Gong, Q. Development of a new nonlinear unified strength theory for geomaterials based on the characteristic stress concept. *Int. J. Geomech.* **2017**, *17*, 04016058. [[CrossRef](#)]
33. Yang, J.; Gu, X.Q. Shear stiffness of granular material at small strains: Does it depend on grain size? *Géotechnique* **2013**, *63*, 165–179. [[CrossRef](#)]
34. Cao, M.; Zhang, Z.; Du, Z.; Wang, L.; Lv, Y.; Zhang, J.; Wang, Y. Experimental Study of Hardening Small Strain Model Parameters for Strata Typical of Zhengzhou and Their Application in Foundation Pit Engineering. *Buildings* **2023**, *13*, 2784. [[CrossRef](#)]
35. Li, L.X.; Liu, J.D.; Li, K.J.; Huang, H.; Ji, X. Study of parameters selection and applicability of HSS model in typical stratum of Jinan. *Rock Soil Mech.* **2019**, *40*, 4021–4029.

36. Shakeel, M.; Ng, C.W. Settlement and load transfer mechanism of a pile group adjacent to a deep excavation in soft clay. *Comput. Geotech.* **2018**, *96*, 55–72. [[CrossRef](#)]
37. Gu, X.Q.; Wu, R.T.; Liang, F.Y.; Gao, G.Y. On HSS model parameters for Shanghai soils with engineering verification. *Rock Soil Mech.* **2021**, *42*, 833–845.
38. Mu, L.; Huang, M. Small strain based method for predicting three-dimensional soil displacements induced by braced excavation. *Tunneling Undergr. Space Tech.* **2016**, *52*, 12–22. [[CrossRef](#)]
39. Jongpradist, P.; Kaewsri, T.; Sawatparnich, A.; Suwansawat, S.; Youwai, S.; Kongkitkul, W.; Sunitsakul, J. Development of tunneling influence zones for adjacent pile foundations by numerical analyses. *Tunneling Undergr. Space Tech.* **2013**, *34*, 96–109. [[CrossRef](#)]
40. Phutthananon, C.; Jongpradist, P.; Jongpradist, P.; Dias, D.; Baroth, J. Parametric analysis and optimization of T-shaped and conventional deep cement mixing column-supported embankments. *Comput. Geotech.* **2020**, *122*, 103555. [[CrossRef](#)]
41. *DG/TJ 508-61-2018*; Technical Code for Excavation Engineering. Tongji University Press: Shanghai, China, 2018; p. 368.
42. Liu, Z.X.; Zhang, H.Q. *PLAXIS Advanced Tutorial*; China Machine Press: Beijing, China, 2015; p. 13.
43. Pei, Y.J.; Zheng, G.; Liu, J.Q. Model test and numerical analysis of diaphragm wall with hinged joints on both sides. *Rock Soil Mech.* **2008**, *29*, 279–284.
44. Liu, Z.X.; Zhang, H.Q. *PLAXIS3D Basic Tutorial*; China Machine Press: Beijing, China, 2021; pp. 131–132.
45. Xu, Z.L. *Elasticity*; Higher Education Press: Beijing, China, 2006; pp. 6–8.
46. Finno, R.J.; Blackburn, J.T.; Roboski, J.F. Three-dimensional effects for supported excavations in clay. *J. Geotech. Geoenviron.* **2007**, *133*, 30–36. [[CrossRef](#)]
47. Li, Z.; Han, M.; Liu, L.; Li, Y.; Yan, S. Corner and partition wall effects on the settlement of a historical building near a supported subway excavation in soft soil. *Comput. Geotech.* **2020**, *128*, 103805. [[CrossRef](#)]
48. Zheng, Y.; Chen, C.; Liu, T.; Shao, Y.; Zhang, Y. Leakage detection and long-term monitoring in diaphragm wall joints using fiber Bragg grating sensing technology. *Tunneling Undergr. Space Tech.* **2020**, *98*, 103331. [[CrossRef](#)]
49. Castaldo, P.; Jalayer, F.; Palazzo, B. Probabilistic assessment of groundwater leakage in diaphragm wall joints for deep excavations. *Tunneling Undergr. Space Tech.* **2018**, *71*, 531–543. [[CrossRef](#)]
50. Shao, Y.; Chen, C.; Lu, Z.; Zheng, Y.; Zhang, Y. An intelligent leakage detection method for diaphragm wall joints based on fiber Bragg grating sensors and intelligent algorithms. *Measurement* **2022**, *197*, 111339. [[CrossRef](#)]
51. Zhang, Y.; Chen, C.; Zheng, Y.; Shao, Y.; Sun, C. Application of fiber Bragg grating sensor technology to leak detection and monitoring in diaphragm wall joints: A field study. *Sensors* **2021**, *21*, 441. [[CrossRef](#)]
52. Xu, Y.; Khan, N.M.; Rehman, H.; Hussain, S.; Khan, R.M.; Emad, M.Z.; Cao, K.; Bin Mohd Hashim, M.H.; Alarifi, S.S.; Cui, R.; et al. Research on Leakage Detection at the Joints of Diaphragm Walls of Foundation Pits Based on Ground Penetrating Radar. *Sustainability* **2022**, *15*, 506. [[CrossRef](#)]
53. *JGJ 120-2012*; Technical Specification for Retaining and Protection of Building Foundation Excavations. China Architecture Press: Beijing, China, 2012; p. 25.

Disclaimer/Publisher’s Note: The statements, opinions and data contained in all publications are solely those of the individual author(s) and contributor(s) and not of MDPI and/or the editor(s). MDPI and/or the editor(s) disclaim responsibility for any injury to people or property resulting from any ideas, methods, instructions or products referred to in the content.